

Diagnosis of bulk phase diagram of non-reciprocal topological lattices by impurity modes

Yanxia Liu¹ and Shu Chen^{1,2,3,*}

¹*Beijing National Laboratory for Condensed Matter Physics,
Institute of Physics, Chinese Academy of Sciences, Beijing 100190, China*

²*School of Physical Sciences, University of Chinese Academy of Sciences, Beijing 100049, China*

³*Yangtze River Delta Physics Research Center, Liyang, Jiangsu 213300, China*

We study the single impurity problem in the non-Hermitian lattice described by the non-reciprocal Su-Schrieffer-Heeger model and obtain the phase diagram of localized bound states induced by the impurity. The existence of analytical results permits us to determine the phase boundaries exactly, which separate regions with different number of bound states. Particularly, in the limit of strong impurity potential, we find that the phase boundaries of mid-gap bound states are identical to the boundaries of topological phase diagrams of the bulk system in the absence of impurity. The existence of correspondence between mid-gap impurity modes and bulk phases indicate that we are able to diagnose the bulk phase diagram of the non-reciprocal topological model by its impurity modes.

I. INTRODUCTION

Non-Hermitian systems have attracted much attention in the past years¹ as some open quantum and optic systems can be effectively modeled by Hamiltonians with non-Hermitian terms^{2–12}. Due to the lack of Hermitian restriction, the non-Hermitian systems possess more types of fundamental nonspatial symmetries than their Hermitian counterpart and thus their topological classification goes beyond the standard ten classes^{13–19}. It was shown that the non-Hermitian systems may exhibit rich exotic phenomena without Hermitian counterparts^{20–36}, e.g., the appearance of novel topological invariants^{27–32}, the existence of non-Hermitian skin effect (NHSE) and breakdown of usual bulk-boundary correspondence in the non-reciprocal lattices^{13,33–49}. A generalized Brillouin zone was proposed to recover the correspondence between the winding of complex energy with periodic boundary and the existence of skin modes with open boundary^{50–53}. The interplay of skin effect and disorder was also studied recently⁵⁴.

In general, nontrivial topological properties of bulk systems can be detected by the behaviors of defects, such as impurities, edges and dislocations^{55–61}. A domain wall configuration is a typical topological defect, which is exponentially localized at the interface between topologically different phases. The open boundary can be viewed as a special domain wall, which separates the bulk state from the vacuum, and the edge state emerges at the boundary if the bulk state is topologically nontrivial. The domain wall in some non-Hermitian topological systems was studied recently and the non-Hermitian effect on the defect state was discussed^{62–69}. While previous works mainly focused on the topological defect on non-Hermitian lattices with spatially distributed gain and loss, the impurity problem in non-reciprocal lattices was rarely addressed. A prominent feature induced by nonreciprocal hopping processes is the emergence of NHSE under open boundary condition (OBC).

The breakdown of bulk-edge correspondence in nonreciprocal lattices suggests the sensitivity of boundary condition for these systems⁶¹. For a single impurity in a one-dimensional (1D) Hermitian lattice, the impurity always induces gap bound states, which are exponentially localized at the impurity, and meanwhile the forward and backward scattering amplitude of the continuous states can be tuned by varying the impurity strength. Particularly, if the strength goes to infinity, the forward scattering is forbidden, and the impurity potential can be effectively treated as a hard-wall boundary (or an OBC). When the impurity strength increases from zero to infinity, a ring lattice with a single impurity can continuously interpolate the system with periodic boundary condition (PBC) to OBC, excluding the gap bound states. However, such an interpolation is broken down for the single impurity problem in the non-reciprocal lattices. The spectrum of continuous states in the limit of infinitely strong impurity potential is obviously different from the spectrum of the open boundary lattice. Therefore, it is very interesting to explore how the impurity potential affects the properties of bound and continuous states in the non-reciprocal topological lattices.

In this work, we focus on a single impurity problem in a non-Hermitian lattice described by a non-reciprocal Su-Schrieffer-Heeger (SSH) model, which has been shown to exhibit NHSE and breakdown of bulk-boundary correspondence. To begin with, we shall first study the single impurity problem in a simple one-band non-reciprocal lattice, which can be solved analytically. Then we analytically solve the impurity problem in the non-reciprocal SSH model and obtain the phase diagram of localized bound states induced by the impurity, in which different phases are distinguished by numbers of bound states. In the limit of large impurity strength, the energy of mid-gap bound state approaches zero and we find that the phase boundaries of mid-gap zero-mode state are identical to the boundaries of bulk topological phase diagrams, indicating that we can detect the bulk phase boundaries of the non-reciprocal topological model by its impurity

modes.

The paper is organized as follows. In Sec. II, we firstly study the single impurity problem in a one-band non-reciprocal chain. With the help of the Green's function method, we can analytically determine the phase diagram for the formation of bound state induced by the impurity. In Sec. III, we study the single impurity problem in the non-reciprocal SSH model, which can be analytically solved by mapping the problem to the impurity problem studied in the previous section. We summarize our results in Sec. IV.

II. SINGLE IMPURITY PROBLEM IN A ONE-BAND NON-RECIPROCAL LATTICE

Firstly, we study a single impurity problem in a simple one-band non-reciprocal lattice, which is described by

$$H = H_0 + V_0 |0\rangle \langle 0|, \quad (1)$$

where V_0 is the strength of the impurity potential on site 0 and H_0 is given

$$H_0 = \sum_n (t_L |n\rangle \langle n+1| + t_R |n+1\rangle \langle n|), \quad (2)$$

where the periodic boundary condition is considered, $t_{R(L)}$ denotes the right (left)-hopping amplitude which can be parameterized as $t_L = te^{-g}$ and $t_R = te^g$ with real t and g . For convenience, we take $t = 1$. The model (2) is also known as the Hatano-Nelson model²¹ without disorder. The non-Hermiticity is induced by the asymmetric hopping processes ($g \neq 0$). Under the periodic boundary condition, the Hamiltonian in the momentum space is given by

$$H_0 = \sum_k h_0(k) |k\rangle \langle k|, \quad (3)$$

with

$$h_0(k) = 2t \cos(k + ig). \quad (4)$$

As the spectrum is complex, one can define a winding number associated with the complex eigenvalue as

$$w = \int_{-\pi}^{\pi} \frac{dk}{2\pi i} \partial_k \ln h_0(k), \quad (5)$$

which gives rise to

$$w = \begin{cases} 1, & g > 0 \\ -1, & g < 0 \end{cases}.$$

The phase with winding number $w = 1$ or -1 belongs to topologically different phase and the transition point locates at $g = 0$, at which the Hamiltonian reduces to a Hermitian one.

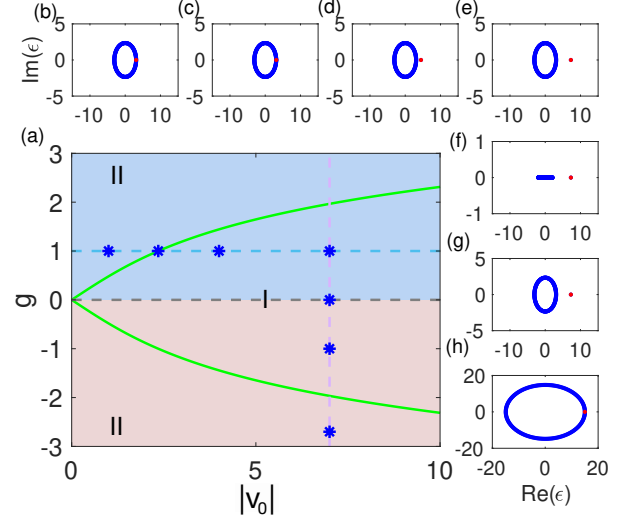


FIG. 1: (a) Phase diagram for localized bound state induced by the impurity in the 1D non-reciprocal lattice. In the regions (I), there is one bound state, and in the region (II), there is no bound state. (b)-(e) The complex-energy spectra with $g = 1$ for $v_0 = 1, 2.35, 4, 7$. (f)-(h) The complex-energy spectra with $v_0 = 7$ for $g = 0, -1, -2.7$.

With the help of Green's function, the wavefunction of the Hamiltonian can be written as

$$\psi(n) = \frac{V_0 \delta_{n,0}}{E - H_0} \psi(0). \quad (6)$$

where E is the eigenvalue of the system. Making a Fourier transformation $\phi(k) = \sum_n e^{-ikn} \psi(n)$ and using Eq.(6), we get

$$\phi(k) = \frac{V_0 \psi(0)}{E - 2t \cos(k + ig)}.$$

Then the inverse Fourier transformation of the above equation gives rise to

$$\begin{aligned} \psi(n) &= \int_{-\pi}^{\pi} \frac{dk}{2\pi} e^{ikn} \phi(k) \\ &= \int_{-\pi}^{\pi} \frac{dk}{2\pi i} \frac{e^{ikn} v_0 \psi(0)}{\epsilon - 2 \cos(k + ig)} \end{aligned}$$

Let $y = e^{ik}$, $v_0 = V_0/t$ and $\epsilon = E/t$, and we can get

$$\psi(n) = \oint \frac{dy}{2\pi e^{-g} i} \frac{v_0 \psi(0)}{(y_2 - y_1)} \left(\frac{y^n}{y - y_1} - \frac{y^n}{y - y_2} \right), \quad (7)$$

where the integral is along a unit circle around the original point and

$$y_{1,2}(\epsilon) = e^g \frac{\epsilon \pm \sqrt{\epsilon^2 - 4}}{2}.$$

When $n = 0$, Eq. (7) becomes

$$-\frac{2\pi i e^g}{v_0} = \oint dy \frac{1}{(y_2 - y_1)} \left(\frac{1}{y - y_1} - \frac{1}{y - y_2} \right). \quad (8)$$

The right part of the above equation can be integrated by using the residue theorem, and the equation has solution only the following condition

$$f(v_0) < e^{-|g|} \quad (9)$$

is fulfilled, where

$$f(v_0) = \frac{\sqrt{v_0^2 + 4} - |v_0|}{2}$$

with $v_0 = V_0/t$. The solution of Eq.(8) gives the eigenenergy of the bound state

$$\epsilon = \text{sgn}(v_0) \sqrt{v_0^2 + 4}, \quad (10)$$

which is real and irrelevant to the parameter g .

By using

$$f(v_0) = e^{-|g|}, \quad (11)$$

we can determine the phase boundary and get the phase diagram for the localized bound state induced by the impurity, which is shown in Fig.5(a). In the region I, there exists a localized bound state, whereas in the region II, no bound state exists. In Fig.1(b)-(h), we display the distribution of energy spectrum for systems with various parameters. For the system in the region II, as shown in Fig.1(b) and (h), only continuous states exist and their eigenvalues form a close circle in the complex plane. For the system in the region I, as shown in Fig.5(d), (e) and (g), there exists a bound state with a real eigenvalue distributed in the real axis outside the circle formed by the continuous states. When $g = 0$, the system reduces to the Hermitian case, as shown in Fig.1(f). The bound state vanishes and the corresponding eigenvalue merges into the circle distribution of continuous states when g locates at the phase boundary, as shown in Fig.1(c). From Fig.1(b)-(e), we can see that the complex eigenvalues of continuous states almost keep invariant with the increase in v_0 . The spectrum of continuous states has no essential change even when $v_0 \rightarrow \infty$, which is obviously different from the real spectra of the open boundary system.

The corresponding wavefunction of the bound state can be written as

$$\psi_b(n) \propto \begin{cases} [\text{sgn}(v_0)e^g f(v_0)]^n & n > 0, \\ [\text{sgn}(v_0)e^{-g} f(v_0)]^{|n|} & n < 0, \end{cases} \quad (12)$$

where $\text{sgn}(v_0)$ is the sign function. When $g = 0$, the bound state decays exponentially and distributes symmetrically around $n = 0$. When $g < 0$, the wavefunction $\psi_b(n)$ distributes asymmetrically and decays more quickly in the region $n > 0$ than in the region $n < 0$, as shown in Fig.2(a3)-(a5). When $g > 0$, the wavefunction decays more quickly in the region $n < 0$ than in the region $n > 0$, as shown in Fig.2(b3)-(b5). From Eq.(12), we can also see that the existence of bound state enforces the constraint condition $e^{|g|}f(v_0) < 1$, otherwise Eq.(12) is not a bound state located around $n = 0$. If

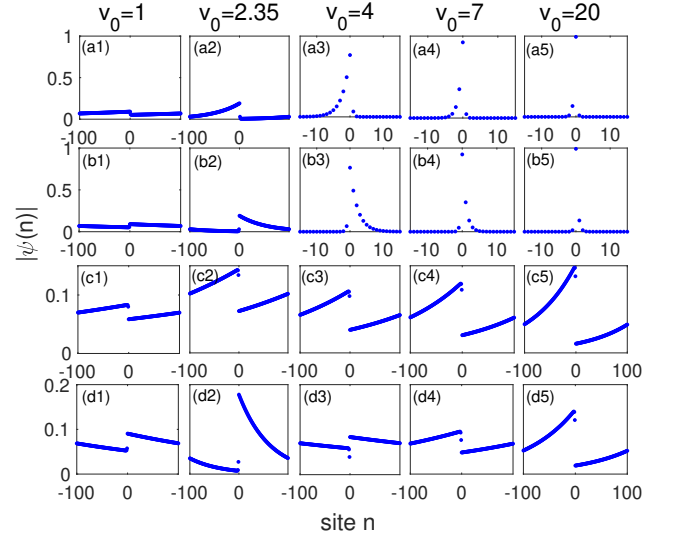


FIG. 2: The distributions of wavefunctions for the impurity model in the one-band non-reciprocal lattice. The columns represent results for five parameters $v_0 = 1, 2.35, 4, 7$ and 20 , respectively. (a1)-(a5) The distributions for the wavefunctions corresponding to the bound state with $g = -1$. (b1)-(b5) The distributions for the wavefunctions corresponding to the bound state with $g = 1$. (c1)-(c5) The distributions of the continuous states with minimum real part of eigenenergies for the system with $g = 1$. (d1)-(d5) The distributions of the continuous states with maximum real part of eigenenergies for system with $g = 1$.

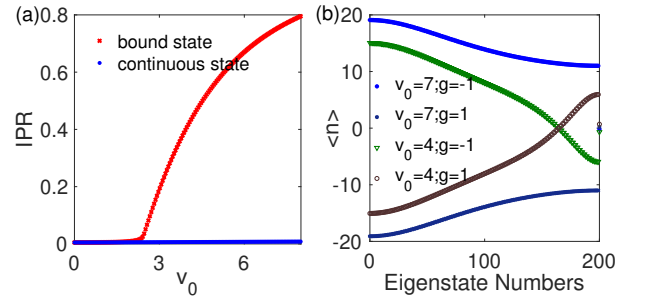


FIG. 3: (a) The IPR for the wavefunction corresponding to the bound state and one of the continuous state versus v_0 for the system with $g = 1$. (b) The mean position of all states for systems with $v_0 = 4, 7$ and $g = \pm 1$.

$f(v_0) \geq e^{-|g|}$, the bound state vanishes and becomes a continuous state, as shown in Fig.2(a1),(a2),(b1) and (b2). For the extended states as shown in the third and fourth rows of Fig.2, no obvious change in the distribution of wavefunction is observed when v_0 crosses the transition point $v_0 = 2.35$. To see clearly the transition between the localized (bound) state and extended (continuous) state, we calculate the inverse participation

ratio (IPR) of the eigenstate $|\psi\rangle$

$$\text{IPR} = \frac{\sum_n |\langle n|\psi\rangle|^4}{(\langle\psi|\psi\rangle)^2}.$$

While $\text{IPR} = 1$ corresponds to a perfectly localized state, $\text{IPR} = 1/N$ corresponds to a fully extended state. We display the IPR for the state corresponding to the bound state versus g in Fig. 3(a), which indicates clearly a transition from an extended to localized state around $v_0 = 2.35$. As a comparison, we also show the IPR for a continuous state in the same figure, which always approaches zero in the whole region of v_0 .

In Fig.2, we have shown that the distribution of wavefunction is asymmetrical with $g \neq 0$. To characterize the asymmetry, we can calculate the mean position $\langle n \rangle = \sum_n \langle \psi | n | \psi \rangle$. While $\langle n \rangle = 0$ corresponds to a symmetrical distribution, $\langle n \rangle > 0$ (< 0) indicates that the wavefunction more likely distributes on the right (left) region of the impurity. The distribution tendency of the bound state is solely determined by $g > 0$ or $g < 0$. For large v_0 , the distribution of extended state also depends on the sign of g . For example, the wave function tends to distribute on the left region of the impurity with $g > 0$ for the large v , as shown in Fig. 2 (c4),(c5),(d4) and (d5). However the extended state can distribute on either the right or left region of the impurity for a given g depending on the choice of state for small v_0 , as shown in Fig.2(b1)-(d1), (b2)-(d2) and (c3)(d3), respectively. To see it clearly, we display the mean position $\langle n \rangle$ for all states of the system with $v_0 = 4, 7$ and $g = \pm 1$ in Fig.3(b). The eigenstates are sorted by the real part of the corresponding eigenenergies. We can see that the mean positions of eigenstates with $g = 1$ and $g = -1$ are symmetric about $\langle n \rangle = 0$.

III. SINGLE IMPURITY PROBLEM IN THE NON-RECIPROCAL SSH MODEL

A. Model and bulk phase diagram

We consider the single impurity problem in a non-reciprocal SSH model with different hopping amplitudes along the right and left hopping directions in the unit cell, as schematically displayed in Fig.4(a). The Hamiltonian is described by

$$\mathcal{H} = \mathcal{H}_{SSH} + V |0, A\rangle \langle 0, A|, \quad (13)$$

where V is the strength of the impurity potential and

$$\mathcal{H}_{SSH} = \sum_n [t(e^{-g} |n, A\rangle \langle n, B| + e^g |n, B\rangle \langle n, A|) + t'(|n, B\rangle \langle n+1, A| + |n+1, A\rangle \langle n, B|)]. \quad (14)$$

Here $te^{\pm g}$ is the right (left) intra-hopping amplitude, t' is the inter-hopping amplitude, A (B) represents the sub-lattice labels and n indicates the n -th cell of the lattice.

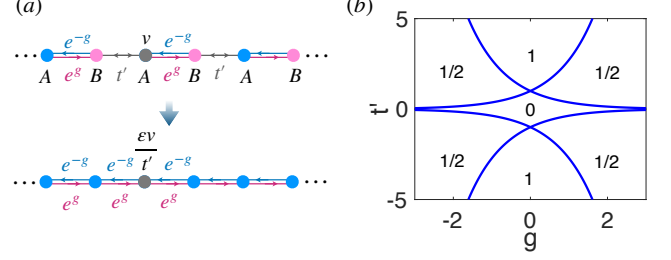


FIG. 4: (a) Schematic diagram of the non-reciprocal SSH model with an impurity. This model can be mapped into a one-band non-reciprocal lattice model with an impurity. (b) The phase diagram of the non-reciprocal SSH model with topologically different phases characterized by the topological invariant $\nu_s = 0, 1/2$ and 1 .

For convenience, we also set $v = V/t$ and $\varepsilon = E/t$. In the following calculation, we take $t = 1$ as the unit of energy.

In the absence of impurity, the non-reciprocal SSH model can be represented in the momentum space via a Fourier transformation with the Hamiltonian given by

$$\mathcal{H}_{SSH}(k) = h_x \sigma_x + h_y \sigma_y,$$

where $h_x = t' \cos k + \cosh g$, $h_y = t' \sin k - i \sinh g$ and $\sigma_{x,y}$ are the Pauli matrices. The phase diagram of the non-reciprocal SSH model can be obtained by following Refs.^{30,33} with the phase boundaries determined by

$$t' = -e^{\pm g} \quad \text{and} \quad t' = e^{\pm g}. \quad (15)$$

The topologically different phases can be distinguished by the topological invariant $\nu_s = \frac{1}{\pi} \int_{-\pi}^{\pi} dk \langle \phi_{\pm}^L | i \partial_k | \phi_{\pm}^R \rangle$, which takes

$$\nu_s = \begin{cases} 1 & |t'| > e^{|g|} \\ \frac{1}{2} & e^{-|g|} < |t'| < e^{|g|} \\ 0 & |t'| < e^{-|g|} \end{cases},$$

where $|\phi_{\pm}^R\rangle$ are the eigenvectors of $\mathcal{H}_0(k)$ and $\langle \phi_{\pm}^L |$ the corresponding left vectors. The phase diagram is shown in the Fig. 4(b).

B. Solution to the impurity problem

Now we study the single impurity problem by solving the stationary Schrödinger equation $\mathcal{H}|\psi\rangle = E|\psi\rangle$ with $|\psi\rangle = \sum_n (\psi_A(n) |n, A\rangle + \psi_B(n) |n, B\rangle)$, which is equivalent to solving the following recurrence equations

$$e^g \psi_A(n-1) + t' \psi_A(n) = \varepsilon \psi_B(n-1), \quad (16)$$

$$t' \psi_B(n-1) + e^{-g} \psi_B(n) + \delta_{x,0} v \psi_A(n) = \varepsilon \psi_A(n), \quad (17)$$

where ε is the eigenvalue. From Eq.(16), we get

$$\psi_B(n) = \frac{e^g}{\varepsilon} \psi_A(n) + \frac{t'}{\varepsilon} \psi_A(n+1). \quad (18)$$

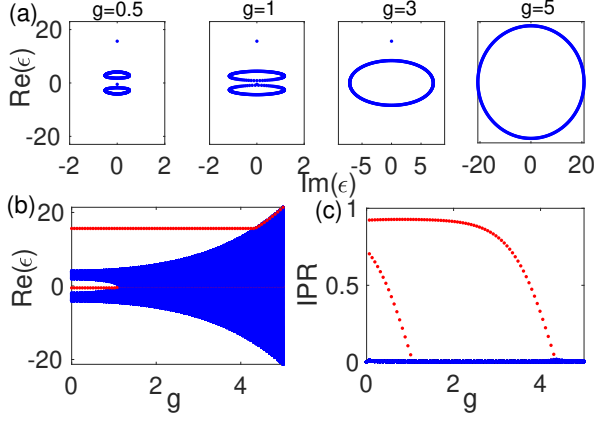


FIG. 5: (a) The complex-energy spectra for the system with $t' = 3$, $v = 15$, $g = 0.5, 1, 3$ and 5 , respectively. (b) The real part of the energy spectra versus g for the system with $t' = 3$ and $v = 15$. (c) IPR for two bound states (red dots) and other continuous states (blue dots).

By substituting it into Eq.(17), we get

$$e^g \psi_A(n-1) + e^{-g} \psi_A(n+1) + \delta_{x,0} \frac{\varepsilon v}{t'} \psi_A(n) = \frac{\varepsilon^2 - t'^2 - 1}{t'} \psi_A(n). \quad (19)$$

It is straightforward to see that the above equation can be mapped into an impurity problem described by Eq.(1) in the previous section, for which the eigenquation $H|\psi\rangle = \epsilon|\psi\rangle$ with $|\psi\rangle = \sum_n \psi(n)|n\rangle$ gives rise to

$$e^g \psi(n-1) + e^{-g} \psi(n+1) + \delta_{x,0} v_0 \psi(n) = \epsilon \psi(n). \quad (20)$$

In comparison with Eq.(19), it is clear that solving Eq.(19) is equivalent to solving Eq.(20) by making the following substitution

$$v_0 = \frac{\varepsilon v}{t'}, \quad (21)$$

$$\epsilon = \frac{\varepsilon^2 - t'^2 - 1}{t'}. \quad (22)$$

Following the procedures described in the previous section, we can analytically determine the condition for the existence of the bound state and get the analytical solutions of the bound state.

Now we can derive the condition for the existence of localized bound state by substituting Eq.(21) into Eq.(9), which gives rise to

$$f\left(\frac{\varepsilon v}{t'}\right) < e^{-|g|}. \quad (23)$$

Similarly by substituting Eq.(21) and Eq.(22) into Eq.(10), we can determine the bound energy of the impurity in the non-reciprocal SSH lattice by solving

$$(\varepsilon^2 - t'^2 - 1)^2 = (\varepsilon v)^2 + 4t'^2,$$

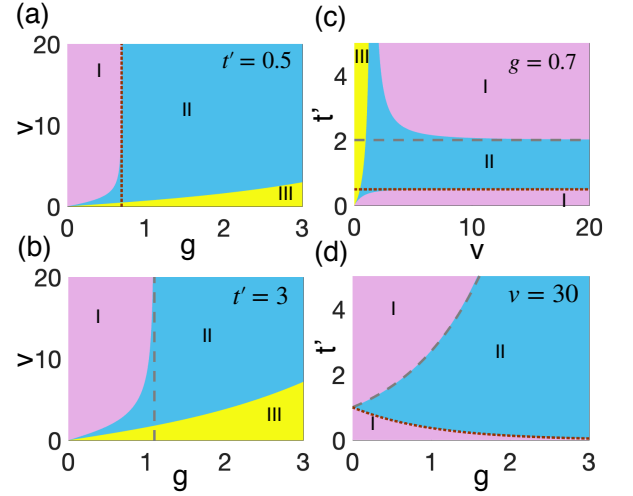


FIG. 6: (a)-(d) Phase diagram for bound states induced by a single impurity in the non-reciprocal SSH model. In the pink (I) and blue (II) regions, there exist two and one localized bound states, respectively, and no bound state exists in the yellow (III) regions. (a) g versus v by fixing $t' = 0.5$, (b) g versus v by fixing $t' = 3$, (c) v versus t' by fixing $g = 0.7$, (d) g versus t' by fixing $v = 30$. The dashed and dotted lines are given by $g = \ln t'$ and $g = -\ln t'$, respectively.

which gives rise to two solutions:

$$\varepsilon_{\pm} = \text{sgn}(\pm v) \sqrt{\frac{v^2 + 2t'^2 + 2 \pm \sqrt{(4 + v^2)(4t'^2 + v^2)}}{2}}.$$

From the above equation, we can see the bound energies ε_+ and ε_- are always real. While ε_+ lies above or below the continuous bands, ε_- lies in the mid-gap region. In the large v limit, we have

$$\varepsilon_- = -\frac{1}{v} |t'^2 - 1|. \quad (24)$$

For $|t'| \neq 1$, the above equation suggests ε_- approaching zero as $v \rightarrow \infty$. While the real bound energies are independent of the parameter g , the complex eigenvalues of the continuous states rely on g . When g keeps increasing and reaches a critical value, ε_- firstly merges into the continuous band accompanying with the disappear of the lower bound state, and then ε_+ merges into the continuous band as g exceeds the second critical value, as shown in Fig.5(a) and (b). Such a transition can be also detected from the change of inverse participation ratio (IPR) for states corresponding to the bound states as shown in Fig.5(c). The IPR of an eigenstate $|\psi\rangle$ is defined by $\text{IPR} = \frac{\sum_n |\langle n|\psi\rangle|^4}{(\langle \psi|\psi\rangle)^2}$. We can find that the mid-gap bound state vanishes at $g = 1.07$, which is close to the topological phase boundary $g = \ln 3 = 1.0986$. The higher bound state vanishes at $g = 4.36$, which is same as the boundary condition obtained by Eq.(23) with $\varepsilon = \varepsilon_+$.

C. Bound-state phase diagram

The phase boundaries of bound-state phase diagram can be determined by

$$f\left(\frac{\varepsilon_- v}{t'}\right) = e^{-|g|} \quad (25)$$

and

$$f\left(\frac{\varepsilon_+ v}{t'}\right) = e^{-|g|}. \quad (26)$$

Different phases in the phase diagram are characterized by the number of bound states. In Fig. 3(a)-(d), we display the phase diagrams with different parameters. In regions I, the parameters satisfy the relations $f(\varepsilon_{\mp} v/t') < e^{-|g|}$, and there exist two localized bound states. In regions II, the parameters satisfy the relations $f(\varepsilon_+ v/t') < e^{-|g|} < f(\varepsilon_- v/t')$, there exists only one bound state. In regions III, no bound state exists as the parameters satisfy the relation $f(\varepsilon_{\pm} v/t') > e^{-|g|}$. In Fig. 6(a) and (b), we display the phase diagram in the parameter space of v versus g with $t' = 0.5$ and 3, respectively. As v increases and goes toward ∞ , the boundary between regions I and region II asymptotically approaches $g = -\ln 0.5$ (dotted line) and $g = \ln 3$ (dashed line), respectively. In Fig. 3(c), the phase diagram is plotted for t' versus v by fixing $g = 0.7$. As v tends to ∞ , the boundaries between regions I and region II approach $t' = \exp(0.7)$ (dashed line) and $t' = \exp(-0.7)$ (dotted line). Fig. 6(d) presents the phase diagram in the parameter space of t' versus g with $v = 30$, which shows the boundaries of the region I and region II almost coinciding with $t' = e^g$ and $t' = e^{-g}$, respectively.

In the limit of $v \rightarrow \infty$, using the expansion of ε_- given by Eq.(24), we can get

$$\begin{aligned} f\left(\frac{\varepsilon_- v}{t'}\right) &= \frac{1}{2}(|t' + \frac{1}{t'}| - |t' - \frac{1}{t'}|), \\ &= \begin{cases} \frac{1}{|t'|} & |t'| > 1, \\ |t'| & |t'| < 1. \end{cases} \end{aligned} \quad (27)$$

In combination with Eq.(25), we get an analytical expression for the phase boundaries between regions with one and two bound states in the large v limit, which reads as

$$|t'| = e^{|g|}, \quad |t'| > 1, \quad (28)$$

$$|t'| = e^{-|g|}, \quad |t'| < 1. \quad (29)$$

The analytical results indicate clearly that the boundaries of zero-mode impurity states are identical to the topological phase boundaries of the periodical bulk system in the absence of impurity given by Eq.(15), therefore we can detect the phase boundary of the bulk system from the boundary of zero-mode bound states induced by a strong impurity potential.

The distribution of bound state wavefunction on A sites are given by

$$\psi_A(n) = \begin{cases} (e^g \beta)^n & n > 0, \\ (e^{-g} \beta)^{|n|} & n < 0, \end{cases} \quad (30)$$

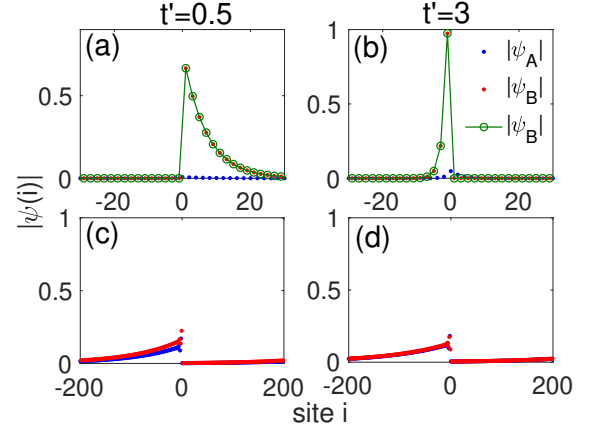


FIG. 7: Distribution of the mid-gap bound state for the system with $v = 60$, $g = 0.4$, (a) $t' = 0.5$ and (b) $t' = 3$, respectively. The green lines correspond to the wavefunction obtained in the limit of $v \rightarrow \infty$. (c) and (d) give the distribution of a continuous state for the same system with $t' = 0.5$ and $t' = 3$, respectively.

where $\beta = \text{sgn}(\frac{\varepsilon_{\pm} v}{t'}) f(\frac{\varepsilon_{\pm} v}{t'})$. The distribution of bound state wavefunction on B sites can be obtained from the recurrence relation (18), which gives rise to

$$\psi_B(n) = e^g \times \begin{cases} \frac{1+t'\beta}{\varepsilon} \psi_A(n) & n \geq 0, \\ \frac{1+t'/\beta}{\varepsilon} \psi_A(n) & n < 0, \end{cases} \quad (31)$$

In the large v limit, we can get a simple analytical expression for the wavefunction of mid-gap bound state. When $|t'| > 1$, we have $\frac{1+t'\beta}{\varepsilon} = -v$ and $\frac{1+t'/\beta}{\varepsilon} = 0$, which suggests the wavefunctions mainly distribute on B sites on the left side of impurity, as the distributions on A site are greatly suppressed by a factor $1/v$. Similarly, when $|t'| < 1$, we have $\frac{1+t'\beta}{\varepsilon} = 0$ and $\frac{1+t'/\beta}{\varepsilon} = -v$, which suggests the wavefunctions mainly distribute on B sites on the right side of impurity. In the limit of $v \rightarrow \infty$, the distributions on A site are completely suppressed, hence the wave function can be written as

$$\psi(n) = \psi_B(n) = \left(-\frac{e^{-g}}{t'}\right)^n, \quad n < 0$$

for $|t'| > 1$ and

$$\psi(n) = \psi_B(n) = (-e^g t')^{|n|}, \quad n > 0$$

for $|t'| < 1$.

In Fig. 7(a) and (b), we display distributions of wavefunction of the mid-gap bound state for systems with $v = 60$, $g = 0.4$, $t' = 0.5$ and $t' = 3$, respectively. The numerical results for $v = 60$ are shown to be almost indiscernible with the analytical results in the infinite v limit. It is clear that the mid-gap bound state locates on different sides of the impurity for the system with $t' > 1$ or $t' < 1$. Therefore, we can distinguish phases corresponding to $\nu_s = 1$ from the phase $\nu_s = 0$ from the different

distributions of the mid-gap state. As a comparison, we also demonstrate the distribution of a continuous state in Fig.7(c) and (d) for the same system with $v = 60$, $g = 0.4$, $t' = 0.5$ and $t' = 3$, respectively. The continuous state distributes asymmetrically and decays slowly from the impurity site. If we change the sign of g , the corresponding continuous states decay from other side of impurity. On the other hand, the distribution of mid-gap state on the left or right side of impurity only depends on the corresponding bulk system is in the phase of $\nu_s = 1$ ($|t'| > 1$) or 0 ($|t'| < 1$), and is not sensitive to the sign of g . More distributions of wavefunctions for the system with various parameters can be found in the appendix.

IV. SUMMARY

In summary, we have studied the single impurity problem in non-reciprocal topological lattices and given the phase diagram of localized bound states. We firstly solve the single impurity problem in a one-band non-reciprocal chain and give the analytical solution of bound state. Due to the interplay of non-reciprocal hopping and impurity potential, the localized bound state occurs only when the potential strength exceeds a critical value. The influence of non-reciprocal hoppings on the wavefunctions of both continuous states and bound state are unveiled. Then by mapping the single-impurity problem in the non-reciprocal SSH model into a single impurity problem in a simple 1D non-reciprocal lattice, we analytically determine the phase diagram and wavefunctions of the localized bound states. In the large impurity strength limit, the eigenvalue of the mid-gap bound state approaches zero and the boundary of zero-mode bound state is found to be identical to the phase boundary of bulk topological phase diagram. The distribution of mid-gap state can also discern topologically different bulk system. The existence of correspondence between impurity zero-mode states and bulk phases suggests that we can detect the bulk phase diagram from behavior of mid-gap impurity modes.

Acknowledgments

The work is supported by NSFC under Grants No.11974413 and the National Key Research and Development Program of China (2016YFA0300600 and 2016YFA0302104).

Appendix A: Distribution of wavefunctions for the non-reciprocal SSH model with a single impurity

In this appendix, we display the distribution of wavefunctions for the system of single impurity in the non-reciprocal SSH lattice with various parameters. In Fig. 8(a) and (b), we display distributions of wavefunctions

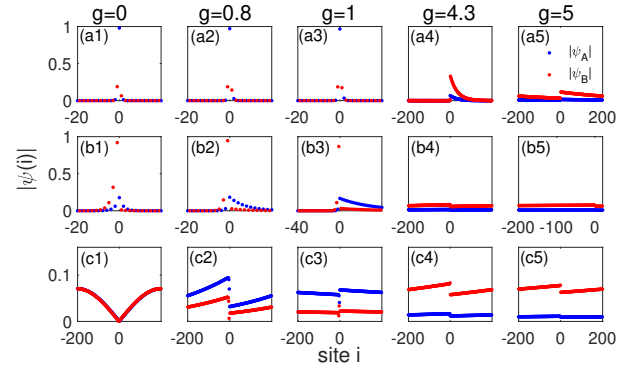


FIG. 8: The distributions of wavefunctions for the impurity model in the non-reciprocal SSH lattice with $t' = 3$ and $v = 15$. The columns represent results for systems with $g = 0, 0.8, 1, 4.3$ and 5 , respectively. (a1)-(a5) The wave functions correspond to eigenenergy ε_+ . (b1)-(b5) The wave functions correspond to eigenenergy ε_- . (c1)-(c5) The wave functions for a randomly chosen extended states.

corresponding to the two bound states for systems with $t' = 3$, $v' = 15$ and various g . When $g = 0$, from the expressions of the bound states in the main text, we can find that the wavefunction on sites A distributes symmetrically around $n = 0$ and decays exponentially, but on sites B distributes asymmetrically, due to the different multipliers of $\psi_B(n)$ in the regions $n > 0$ and $n < 0$. When $g \neq 0$, the wavefunction $\psi_A(n)$ distributes asymmetrically and decays more quickly in one of sides of the impurity than in the other side, as shown in Fig.8(a) and (b). The bound state consists of two exponentially decaying distributions on sites A and B , respectively. When g exceeds the first critical value ($g_{c1} \approx 1.1$), the mid-gap bound state vanishes. Further increasing g and exceeding the second critical value ($g_{c2} \approx 4.36$), the bound state corresponding to ε_+ also vanishes. As a comparison, we demonstrate the distribution of a continuous state in Fig.8(c) and find no obvious changes when g exceeds both critical values. The distributions of wavefunctions are consistent with the results of IPR shown in Fig.2(c) of the main text. Distributions of bound-state wavefunctions for systems in the region of $t' < 1$ are found to display similar behaviors.

Fig.9(a1)-(a5) show the distributions of wavefunctions corresponding to the eigenenergy ε_+ with $t' = 0.5$, $g = 0.4$ and various v . The formation of the bound states requires $f(\varepsilon_+ v/t') < e^{-|g|}$, otherwise there is no bound state. For $v = 0.2$, no bound state exists and the corresponding state is a continuous state [See Fig. 9 (a1)]. When v exceeds a critical value, a bound state appears [See Figs.9 (a2)-(a5)]. The probability of distributions on B sites (ψ_B) decreases with the increase of v . In the limit of $v \rightarrow \infty$, ψ_B is entirely suppressed and only ψ_A exists. The wavefunctions for systems with $t' > 1$ are found to display similar behaviors. Figs.9(b1)-(b5) show the distributions of wavefunctions corresponding to the eigenenergy ε_- with $t' = 0.5$, $g = 0.4$ and various

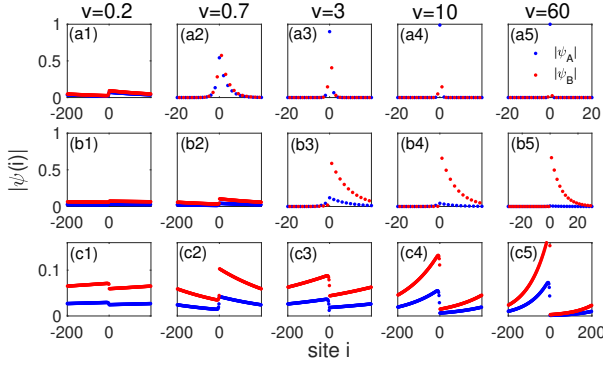


FIG. 9: The distributions of wavefunctions for the impurity model in the non-reciprocal SSH lattice with $t' = 0.5$ and $g = 0.4$. The columns represent results for systems with $v = 0.2, 0.7, 3, 10$ and 60 , respectively. (a1)-(a5) The wave functions correspond to eigenenergy ε_+ . (b1)-(b5) The wave functions correspond to eigenenergy ε_- . (c1)-(c5) The wave functions for a randomly chosen extended states.

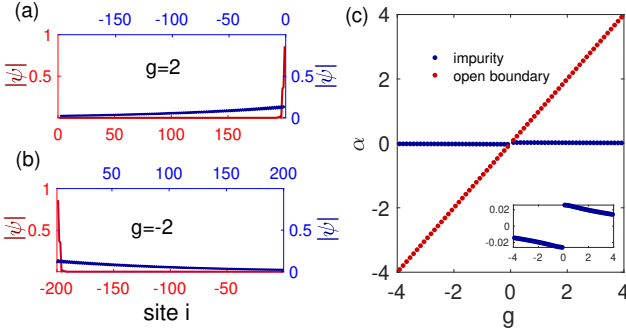


FIG. 10: The distribution of the continuous state for impurity model (blue solid line) and open-boundary model (red solid line) with $t' = 3$, (a) $g = 2$ and (b) $g = -2$, respectively. The parameter $v = 200$ for the impurity model and the site number is 400 . (c) The exponential decay constant for the distribution of wavefunction of non-reciprocal SSH model with open boundary condition (red dots) and with an impurity (blue dots).

v . The formation of the mid-gap bound states requires $f(\varepsilon_- v/t') < e^{-|g|}$. For $v = 0.2$ and 0.7 , no mid-gap bound state exists and the corresponding state is a continuous state, as shown in Fig. 9 (b1) and (b2). When v

exceeds the second critical value, a mid-gap bound state appears as shown in Fig.9 (b3)-(b5). The probability of distributions on A sites (ψ_A) decreases with the increase of v . In the limit of $v \rightarrow \infty$, ψ_A is completely suppressed and the wavefunction only distributes on B sites with ψ_B localized at the right side of the impurity. The extended state may distribute on either the right or left region of the impurity for a given g and small v , as shown in Fig.9(a1)-(c1). In the large v limit, the extended state for $g > 0$ tends to distribute on the left region of the impurity, as shown in Fig.9(c5).

For the large v case, the distribution tendency of the continuous state is solely determined by $g > 0$ or $g < 0$, which is similar to the skin effect in the open boundary case. However, the distribution for the impurity model decays very slowly and distribute in the whole region of the lattice, which is very different from the skin effect. Here we would like to compare their difference quantitatively. The non-reciprocal SSH model under the open boundary condition can be mapped to a Hermitian SSH model by a similarity transformation, $\mathcal{H}'_0 = U^{-1}\mathcal{H}_0U$, where \mathcal{H}'_0 is a standard SSH model i.e., the Hamiltonian \mathcal{H}_0 with $g = 0$. Here U can be taken as a diagonal matrix whose diagonal elements are $\{1, e^g, e^{2g}, e^{3g}, \dots, e^{Ng}\}$. The wavefunction of non-reciprocal SSH model can be written as $|\psi\rangle = U|\psi'\rangle$, where $|\psi'\rangle$ satisfies $\mathcal{H}'_0|\psi'\rangle = E|\psi'\rangle$. As $|\psi'\rangle$ is always uniformly distributed except of the zero-mode state, the 'non-Hermitian skin effect' can be understood as a result of the transformation U . When the $g < 0$ ($g > 0$), the eigenstates are localized at the left (right) edge of the chain, as shown in Fig.10 (b) and (a) (red solid lines). In Fig. 10(c), we use red dots to represent the exponential decay constant $\alpha = \ln(|\psi_A(n)|/|\psi_A(n-1)|) \simeq g$ for the skin state of the system with OBC. For the impurity system with large v , the distributions of continuous states decay exponentially but very slowly from the right or left impurity site and the direction depends on the sign of g , as shown in Fig.10(a) and (b) by the blue solid lines. In Fig. 10(c), we use blue dots to denote the exponential decay constant $\alpha = \ln(|\psi_A(n)|/|\psi_A(n-1)|)$ for the impurity model, which shows the continuous states decaying much more slowly than the skin states under open boundary condition. The exponential decay constant $\alpha = 0.0175$ for $g = 2$ and $\alpha = -0.0175$ for $g = -2$.

* Electronic address: schen@iphy.ac.cn

¹ N. Moiseyev, *Non-Hermitian Quantum Mechanics*, CAMBRIDGE UNIVERSITY PRESS, 1st edition, 2011.

² L. Lu, J. D. Joannopoulos, and M. Soljacic, Topological photonics, *Nat Photon*, **8**, 821 (2014).

³ T. Ozawa, H. M. Price, A. Amo, N. Goldman, M. Hafezi, L. Lu, M. Rechtsman, D. Schuster, J. Simon, O. Zilberberg, and I. Carusotto, Topological photonics. *Rev. Mod. Phys.*

91, 015006 (2019).

⁴ A. Guo, G. J. Salamo, D. Duchesne, R. Morandotti, M. Volatier-Ravat, V. Aimez, G. A. Siviloglou, and D. N. Christodoulides. Observation of PT-symmetry breaking in complex optical potentials, *Phys. Rev. Lett.* **103**, 093902 (2009).

⁵ B. Peng, S. K. Ozdemir, F. Lei, F. Monifi, M. Gianfreda, G. L. Long, S. Fan, F. Nori, C. M. Bender, and

- L. Yang, Parity-time-symmetric whispering-gallery microcavities, *Nature Physics*, **10**, 394 (2014).
- ⁶ B. Zhen, C. W. Hsu, Y. Igarashi, L. Lu, I. Kaminer, A. Pick, S.-L. Chua, J. D. Joannopoulos, and M. Soljacic, Spawning rings of exceptional points out of dirac cones. *Nature*, **525**, 354 (2015).
 - ⁷ K. Ding, G. Ma, M. Xiao, Z. Q. Zhang, and C. T. Chan. Emergence, coalescence, and topological properties of multiple exceptional points and their experimental realization, *Phys. Rev. X*, **6**, 021007 (2016).
 - ⁸ J. Doppler, A. A. Mailybaev, J. Bohm, U. Kuhl, A. Girschik, F. Libisch, T. J. Milburn, P. Rabl, N. Moiseyev, and S. Rotter, Dynamically encircling an exceptional point for asymmetric mode switching, *Nature* **537**, 76 (2016).
 - ⁹ H. Xu, D. Mason, Luyao Jiang, and J. G. E. Harris, Topological energy transfer in an optomechanical system with exceptional points, *Nature*, **537**, 80 (2016).
 - ¹⁰ B. Midya, H. Zhao, and L. Feng, Nonhermitian photonics promises exceptional topology of light, *Nature Communications*, **9**, 2674 (2018).
 - ¹¹ V. M. Martinez Alvarez, J. E. Barrios Vargas, M. Berdakin, and L. E. F. Foa Torres, Topological states of non-Hermitian systems, *Eur. Phys. J. Spec. Top.* **227**, 1295 (2018).
 - ¹² A. Ghatak and T. Das, New topological invariants in non-Hermitian systems, *J. Phys.: Condens. Matter* **31**, 263001 (2019).
 - ¹³ Z. Gong, Y. Ashida, K. Kawabata, K. Takasan, S. Higashikawa, and M. Ueda, Topological Phases of Non-Hermitian Systems, *Phys. Rev. X* **8**, 031079 (2018).
 - ¹⁴ C. Liu, H. Jiang, and S. Chen, Topological classification of non-Hermitian systems with reflection symmetry, *Phys. Rev. B* **99**, 125103 (2019).
 - ¹⁵ K. Kawabata, K. Shiozaki, M. Ueda, and M. Sato, Symmetry and Topology in Non-Hermitian Physics, *Phys. Rev. X* **9**, 041015 (2019).
 - ¹⁶ H. Zhou and J. Y. Lee, Periodic table for topological bands with non-Hermitian symmetries, *Phys. Rev. B* **99**, 235112 (2019).
 - ¹⁷ S. Lieu, Topological symmetry classes for non-Hermitian models and connections to the Bosonic Bogoliubov-Cde Gennes equation, *Phys. Rev. B* **98**, 115135 (2018).
 - ¹⁸ K. Kawabata, S. Higashikawa, Z. Gong, Y. Ashida, and M. Ueda, Topological unification of time-reversal and particle-hole symmetries in non-Hermitian physics, *Nat. Commun.* **10**, 297 (2019).
 - ¹⁹ H. C. Wu, L. Jin, and Z. Song, Inversion symmetric non-Hermitian Chern insulator, *Phys. Rev. B* **100**, 155117 (2019).
 - ²⁰ Y. Xu, S.-T. Wang, and L.-M. Duan, Weyl Exceptional Rings in a Three-Dimensional Dissipative Cold Atomic Gas, *Phys. Rev. Lett.* **118**, 045701 (2017).
 - ²¹ N. Hatano and D. R. Nelson, Localization Transitions in Non-Hermitian Quantum Mechanics, *Phys. Rev. Lett.* **77**, 570 (1996).
 - ²² N. Hatano and D. R. Nelson, Vortex pinning and non-Hermitian quantum mechanics, *Phys. Rev. B* **56**, 8651 (1997).
 - ²³ M. S. Rudner and L. S. Levitov, Topological Transition in a Non-Hermitian Quantum Walk, *Phys. Rev. Lett.* **102**, 065703 (2009).
 - ²⁴ K. Esaki, M. Sato, K. Hasebe, and M. Kohmoto, Edge states and topological phases in non-Hermitian systems, *Phys. Rev. B* **84**, 205128 (2011).
 - ²⁵ B. Zhu, R. Lü, and S. Chen, PT symmetry in the non-Hermitian Su-Schrieffer-Heeger model with complex boundary potentials, *Phys. Rev. A* **89**, 062102 (2014).
 - ²⁶ C. Yuce, Topological phase in a non-Hermitian PT symmetric system, *Phys. Lett. A* **379**, 1213 (2015).
 - ²⁷ T. E. Lee, Anomalous Edge State in a Non-Hermitian Lattice, *Phys. Rev. Lett.* **116**, 133903 (2016).
 - ²⁸ D. Leykam, K. Y. Bliokh, C. Huang, Y. D. Chong, and F. Nori, Edge Modes, Degeneracies, and Topological Numbers in Non-Hermitian Systems, *Phys. Rev. Lett.* **118**, 040401 (2017).
 - ²⁹ H. Shen, B. Zhen, and L. Fu, Topological Band Theory for Non-Hermitian Hamiltonians, *Phys. Rev. Lett.* **120**, 146402 (2018).
 - ³⁰ C. Yin, H. Jiang, L. Li, R. Lü and S. Chen, Geometrical meaning of winding number and its characterization of topological phases in one-dimensional chiral non-Hermitian systems, *Phys. Rev. A* **97**, 052115 (2018).
 - ³¹ S. Lieu, Topological phases in the non-Hermitian Su-Schrieffer-Heeger model, *Phys. Rev. B* **97**, 045106 (2018).
 - ³² H. Jiang, C. Yang, and S. Chen, Topological invariants and phase diagrams for one-dimensional two-band non-Hermitian systems without chiral symmetry, *Phys. Rev. A* **98**, 052116 (2018).
 - ³³ S. Yao and Z. Wang, Edge States and Topological Invariants of Non-Hermitian Systems, *Phys. Rev. Lett.* **121**, 086803 (2018).
 - ³⁴ V. M. Martinez Alvarez, J. E. Barrios Vargas, and L. E. F. Foa Torres, Non-hermitian robust edge states in one dimension: Anomalous localization and eigenspace condensation at exceptional points, *Phys. Rev. B* **97**, 121401(R) (2018).
 - ³⁵ Y. Xiong, Why does bulk boundary correspondence fail in some non-hermitian topological models, *J. Phys. Commun.* **2**, 035043 (2018).
 - ³⁶ F. K. Kunst, E. Edvardsson, J. C. Budich, and E. J. Bergholtz, Biorthogonal bulk-boundary correspondence in non-hermitian systems, *Phys. Rev. Lett.* **121**, 026808 (2018).
 - ³⁷ S. Yao, F. Song, and Z. Wang, Non-hermitian chern bands, *Phys. Rev. Lett.* **121**, 136802 (2018).
 - ³⁸ L. Jin and Z. Song, Bulk-boundary correspondence in non-hermitian systems, *Phys. Rev. B* **99**, 081103(R) (2019).
 - ³⁹ C. H. Lee and R. Thomale, Anatomy of skin modes and topology in non-Hermitian systems, *Phys. Rev. B* **99**, 201103(R) (2019).
 - ⁴⁰ K. Kawabata, K. Shiozaki, and M. Ueda, Anomalous helical edge states in a non-hermitian chern insulator, *Phys. Rev. B*, **98**, 165148, (2018).
 - ⁴¹ C. H. Lee, L. Li, and J. Gong, Hybrid higher-order skin-topological modes in non-reciprocal systems, *Phys. Rev. Lett.* **123**, 016805 (2019).
 - ⁴² L. Herviou, J. H. Bardarson, and N. Regnault, Defining a bulk-edge correspondence for non-Hermitian Hamiltonians via singular-value decomposition, *Phys. Rev. A* **99**, 052118 (2019).
 - ⁴³ W. B. Rui, Y. X. Zhao, Andreas P. Schnyder, Classification of massive Dirac models with generic non-Hermitian perturbations, *Phys. Rev. B* **99**, 241110(R) (2019).
 - ⁴⁴ F. Song, S. Yao, and Z. Wang, Non-Hermitian Topological Invariants in Real Space, *Phys. Rev. Lett.* **123**, 246801 (2019).
 - ⁴⁵ S. Longhi, Probing non-Hermitian Skin Effect and non-Bloch Phase Transitions, *Phys. Rev. Research* **1**, 023013 (2019).

- (2019).
- ⁴⁶ H. Jiang, R. Lu, and S. Chen, Topological invariants, zero mode edge states and finite size effect for a generalized non-reciprocal Su-Schrieffer-Heeger model, arXiv:1906.04700 (2019).
 - ⁴⁷ Z. Ozcakmakli Turker and C. Yuce, Open and closed boundaries in non-Hermitian topological systems, Phys. Rev. A **99**, 022127 (2019).
 - ⁴⁸ L. Xiao, T. Deng, K. Wang, G. Zhu, Z. Wang, W. Yi, and P. Xue, Observation of non-Hermitian bulk-boundary correspondence in quantum dynamics, arXiv:1907.12566 (2019).
 - ⁴⁹ X. R. Wang, C. X. Guo, and S. P. Kou, Defective Edge States and Anomalous Bulk-Boundary Correspondence in non-Hermitian Topological Systems, Phys. Rev. B **101**, 121116 (2020).
 - ⁵⁰ K. Yokomizo and S. Murakami, Non-Bloch Band Theory of Non-Hermitian Systems, Phys. Rev. Lett. **123**, 066404 (2019).
 - ⁵¹ K. Zhang, Z. Yang, C. Fang, Correspondence between winding numbers and skin modes in non-hermitian systems, arXiv:1910.01131 (2019).
 - ⁵² Z. Yang, K. Zhang, C. Fang, and J. Hu, Auxiliary generalized Brillouin zone method in non-Hermitian band theory, arXiv:1912.05499 (2019).
 - ⁵³ N. Okuma, K. Kawabata, K. Shiozaki, and M. Sato, Topological Origin of Non-Hermitian Skin Effects, arXiv:1910.02878 (2019).
 - ⁵⁴ H. Jiang, L. Lang, C. Yang, S. Zhu, and S. Chen, Interplay of non-Hermitian skin effects and Anderson localization in nonreciprocal quasiperiodic lattices, Phys. Rev. B **100**, 054301(2019).
 - ⁵⁵ J. C. Y. Teo and C. L. Kane, Topological defects and gapless modes in insulators and superconductors, Phys. Rev. B **82**, 115120 (2010).
 - ⁵⁶ J. Lu, W.-Y. Shan, H.-Z. Lu, and S.-Q. Shen, Non-magnetic impurities and in-gap bound states in topological insulators, New J. Phys. **13**, 103016 (2011).
 - ⁵⁷ L.-J. Lang and S. Chen, Topologically protected mid-gap states induced by impurity in one-dimensional superlattices, J. Phys. B: At. Mol. Opt. Phys. **47**, 065302 (2014).
 - ⁵⁸ R.-J. Slager, L. Rademaker, J. Zaanen, and L. Balents, Impurity-bound states and Green's function zeros as local signatures of topology, Phys. Rev. B **92**, 085126 (2015).
 - ⁵⁹ L. Kimme and T. Hyart, Existence of zero-energy impurity states in different classes of topological insulators and superconductors and their relation to topological phase transitions, Phys. Rev. B **93**, 035134 (2016).
 - ⁶⁰ C. Liu, and S. Chen, Topological classification of defects in non-Hermitian systems, Phys. Rev. B **100**, 144106(2019).
 - ⁶¹ D. S. Borgnia, A. J. Kruchkov, and R.-J. Slager, Non-Hermitian Boundary Modes, Phys. Rev. Lett. **124**, 056802 (2020).
 - ⁶² H. Schomerus, Topologically protected midgap states in complex photonic lattices, Opt. Lett. **38**, 1912 (2013).
 - ⁶³ S. Longhi, Bound states in the continuum in PT-symmetric optical lattices, Opt. Lett. **39**, 1697 (2014).
 - ⁶⁴ S. Malzard, C. Poli, and H. Schomerus, Topologically Protected Defect States in Open Photonic Systems with Non-Hermitian Charge-Conjugation and Parity-Time Symmetry, Phys. Rev. Lett. **115**, 200402 (2015).
 - ⁶⁵ C. Yuce, Edge states at the interface of non-Hermitian systems, Phys. Rev. A **97**, 042118 (2018).
 - ⁶⁶ L. Lang, Y. Wang, H. Wang, and Y. Chong, Effects of non-Hermiticity on Su-Schrieffer-Heeger defect states, Phys. Rev. B **98**, 094307 (2018).
 - ⁶⁷ T. S. Deng and W. Yi, Non-Bloch topological invariants in a non-Hermitian domain-wall system, , Phys. Rev. B **100**, 035102 (2019).
 - ⁶⁸ Y.-J. Wu and J. Hou, Symmetry-protected localized states at defects in non-Hermitian systems, Phys. Rev. A **99**, 062107 (2019).
 - ⁶⁹ M. Ezawa, Non-Hermitian boundary and interface states in nonreciprocal higher-order topological metals and electrical circuits, Phys. Rev. B **99**, 121411(R) (2019).